1-2016

M2 Internal Tides and Their Observed Wavenumber Spectra from Satellite Altimetry

Richard D. Ray
NASA Goddard Space Flight Center, richard.ray@nasa.gov

Edward D. Zaron
Portland State University, ezaron@pdx.edu

Citation Details

Ray, R. D., & Zaron, E. D. (2016). M2 Internal Tides and Their Observed Wavenumber Spectra from Satellite Altimetry*. Journal Of Physical Oceanography, 46(1), 3-22. doi:10.1175/JPO-D-15-0065.1

M_2 Internal Tides and Their Observed Wavenumber Spectra from Satellite Altimetry*

R. D. RAY

NASA Goddard Space Flight Center, Greenbelt, Maryland

E. D. ZARON

Department of Civil and Environmental Engineering, Portland State University, Portland, Oregon

(Manuscript received 2 April 2015, in final form 14 September 2015)

ABSTRACT

A near-global chart of surface elevations associated with the stationary M_2 internal tide is empirically constructed from multimission satellite altimeter data. An advantage of a strictly empirical mapping approach is that results are independent of assumptions about ocean wave dynamics and, in fact, can be used to test such assumptions. A disadvantage is that present-day altimeter coverage is only marginally adequate to support mapping such short-wavelength features. Moreover, predominantly north–south ground-track orientations and contamination from nontidal oceanographic variability can lead to deficiencies in mapped tides. Independent data from *Cryosphere Satellite-2* (*CryoSat-2*) and other altimeters are used to test the solutions and show positive reduction in variance except in regions of large mesoscale variability. The tidal fields are subjected to two-dimensional wavenumber spectral analysis, which allows for the construction of an empirical map of modal wavelengths. Mode-1 wavelengths show good agreement with theoretical wavelengths calculated from the ocean's mean stratification, with a few localized exceptions (e.g., Tasman Sea). Mode-2 waves are detectable in much of the ocean, with wavelengths in reasonable agreement with theoretical expectations, but their spectral signatures grow too weak to map in some regions.

1. Introduction

Satellite altimetry has given us a unique near-global perspective on deep-ocean internal tides. It has pinpointed wave-generation regions and has shown that low-mode waves are capable of propagating thousands of kilometers with relatively little energy loss (e.g., Ray and Mitchum 1996; Cummins et al. 2001; Zhao et al. 2012). It has allowed testing of theoretical issues related to dissipation mechanisms (e.g., Zhao et al. 2010), and it has provided an invaluable dataset for testing numerical models (Niwa and Hibiya 2001, 2004; Arbic et al. 2010; Shriver et al. 2012).

Yet the altimetric view of internal tides is also limited by its fundamental measurement—surface elevation only—and by its temporal and spatial undersampling. The altimeter measurement is nearly everywhere dominated by the first baroclinic mode. While higher modes are certainly detectable in much of the ocean, their signals are suppressed relative to what might be measured within the water column. Similarly, an altimeter's temporal undersampling means that the stationary, phase-locked waves are the easiest to extract and study, leaving a possibly very significant nonstationary part neglected. Finally, spatial undersampling often forces us to study a limited one-dimensional (along track) picture. This paper addresses one aspect of the latter problem as we attempt to map in two dimensions the sea surface heights (SSH) of the M_2 internal tide.

The spatial undersampling problem is gradually being alleviated by more and more satellite missions with differing ground tracks (Zhao et al. 2011). For example, Fig. 1 shows track coverage for a region near the Hawaiian Ridge arising from the following missions:

* Supplemental information related to this paper is available at the Journals Online website: http://dx.doi.org/10.1175/JPO-D-15-0065.s1.

Corresponding author address: R. D. Ray, NASA/GSFC, Code 698, Greenbelt, MD 20771.
E-mail: richard.ray@nasa.gov

DOI: 10.1175/JPO-D-15-0065.1

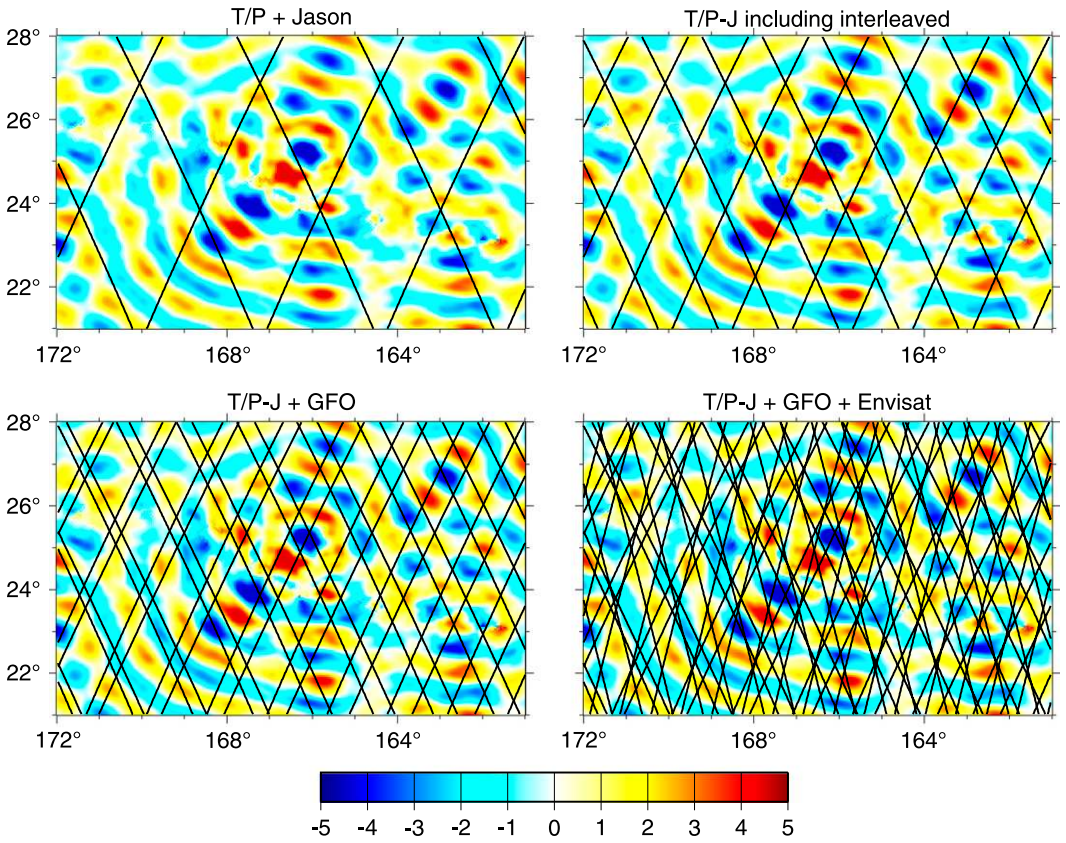

FIG. 1. Satellite ground track coverage near the Hawaiian Ridge from four altimeter missions (and their successors), overlain atop sea surface heights of the stationary M_2 internal tide (in-phase part, in cm) according to the numerical model of Zaron and Egbert (2006). The tidal SSH of the model compares reasonably well with altimetry, particularly near the generation sites (Zaron and Egbert 2014). The track coverage from the combined missions (lower right panel) is marginally adequate to map the short scales of the SSH field. Ray and Cartwright (2001) had previously attempted to map energy fluxes using only T/P data (upper-left panel)—a somewhat quixotic endeavor, although at that time there were expectations of long-crested plane waves emanating from the ridge, which would have been more easily sampled along sparse tracks.

(i) TOPEX/Poseidon (T/P), *Jason-1*, and *Jason-2*; (ii) the extended missions of T/P and *Jason-1* when those satellites were shifted into an interleaved ground track; (iii) *Geosat* and *Geosat Follow-On* (*GFO*); and (iv) *ERS-1*, *ERS-2*, and *Envisat*. For all four of these track patterns, sufficiently long time series of altimeter data have now been collected to allow tides to be estimated independently point by point at individual locations along the tracks (at least for lunar constituents) with subcentimeter precisions. The full satellite coverage in the lower-right panel of Fig. 1 is marginally adequate to map the surface expression of the low-mode internal tide.

Dushaw (2002) and Dushaw et al. (2011) have shown that spatial undersampling can be mostly overcome by constraining the mapped elevation fields to be consistent with the theoretical frequency–wavenumber spectrum of free waves in a flat-bottom ocean with a climatological-mean stratification. With this approach, Dushaw et al. (2011) produced quite reasonable maps of first-mode M_2 elevations in the vicinity of the Hawaiian Ridge, based on data from only the T/P and Jason-series satellite (T/P-J) missions. Zhao et al. (2012) have also successfully mapped internal tide elevations by exploiting the known modal wavelengths associated with the mean stratification. They have considerably extended a localized plane wave fitting approach (Ray and Cartwright 2001) to relatively high resolution based on all the satellites shown in Fig. 1.

There are, nonetheless, grounds for investigating how well the altimeter data alone can map these two-dimensional SSH fields without reliance on assumptions about modal decompositions or possible interactions with the mean flow or even knowledge of ocean stratification. It is always profitable to analyze data with as few dynamical assumptions as possible, that is,

TABLE 1. Satellite altimeter data used.

Satellites	Timespan	No. repeat cycles	Repeat period (d)	No. orbits per repeat	Inclination (°)	M_2 Alias (d)
T/P-J	1992–2009	623	9.9156	127	66.04	62.1
T/P-J interlaced	2001–12	223	9.9156	127	66.04	62.1
GFO	2000–07	187	17.0505	244	108.06	317.1
ERS–*Envisat*	1995–2010	162	35.0000	501	98.40	94.5

to analyze data in what Dushaw et al. (2011) called ''discovery mode.'' In the end, the data may be too limited to avoid invoking dynamical assumptions and indeed in the analysis to follow we find certain deficiencies. Some of these may well be ameliorated in the future as more and more altimeter data are collected, especially after planned missions with wide-swath altimetry are realized (e.g., Durand et al. 2010; Fu and Ubelmann 2014).

2. Tidal analysis of along-track altimetry

Along-track tidal analysis of altimeter data is by now a well-studied technique, and its strengths and weaknesses are understood (e.g., Carrère et al. 2004). This section addresses certain aspects warranting special attention for the problem of mapping internal tides.

The satellite altimeter data used in this analysis are summarized in Table 1. For the most part, standard altimeter corrections and adjustments were applied to these data. A prior model of the barotropic ocean tide and its associated crustal deformation [Goddard/Grenoble Ocean Tide, version 4.8 (GOT4.8); see the appendix of Ray (2013)] was used as well as an elastic model of the solid body tide. Any residual tidal signal is then presumably either the baroclinic tide or barotropic model error.

a. Correction for nontidal variance

Among the weaknesses of along-track analyses of altimetry are problems associated with the temporal aliasing of tidal signals into long periods. Real ocean variability at those alias periods can leak into the altimetric tidal estimates, leading to a challenging problem of disentangling tidal from nontidal signals. A longer time series of altimetry does slowly reduce the problem somewhat (see below), at least to the extent the tidal signal is a line spectrum. But in regions of intense mesoscale variability the leakage of nontidal variability can overwhelm tiny signals associated with internal tides. In addition, it is conceivable—indeed it is likely—that intense mesoscale variability weakens any phase-locked nature of internal tides, at least relative to that observed in quieter regions, thus further hampering extraction of useful signal.

This section follows up on a suggestion (Ray and Byrne 2010) for reducing leakage of nontidal energy into altimetric tidal solutions by using a model of oceanic SSH anomalies as a prior correction. It is unlikely that any such model can be sufficiently accurate for this task unless it itself is based on altimetry. We use the multimission ¼° global SSH fields created by the Archiving, Validation, and Interpretation of Satellite Oceanographic Data (AVISO) center, specifically their Data Unification and Altimeter Combination System (DUACS) version DT-2010 (AVISO 2014). These SSH data were produced weekly by objective mapping of multimission altimeter data (Dibarboure et al. 2011). Occasionally as many as four contemporaneous missions were available for these fields, although years 1992–2000 relied on only two missions.

It is worth addressing this proposed ''mesoscale correction'' in some detail in both space and wavenumber domains. Figure 2 shows the effect of applying the nontidal AVISO correction to observed SSH wavenumber spectra for four T/P-J tracks in the South Pacific. In this figure the black curves are spectra computed by standard methods (e.g., Stammer 1997), averaging individual spectra from over several hundred repeat passes of the altimeter. All standard corrections, including for the barotropic tide, have been applied. The red curves show the spectra after the AVISO correction. All four of the tracks show evidence of semidiurnal internal tides since they display a peak, or at least a shoulder, in the 120–160-km wave band, similar to internal tide signatures that have been previously published (Ray and Zaron 2011). The AVISO correction reduces much of the variance in wavenumbers below and slightly into the internal tide band, and the resulting spectra more clearly delineate the tidal peaks. Note too that a simple high-pass wavenumber filter would not be so effective, since there is spectral overlap between the eddy field and the tidal band.

Effects in the space domain are shown in Fig. 3 for three different tracks specially selected because they cross a region of both strong internal tides, generated either near the Madagascar Plateau or the Southern Mascarene Plateau, as well as high mesoscale variability from the Antarctic Circumpolar Current (ACC); for each track the internal tide dominates in the north, the ACC dominates

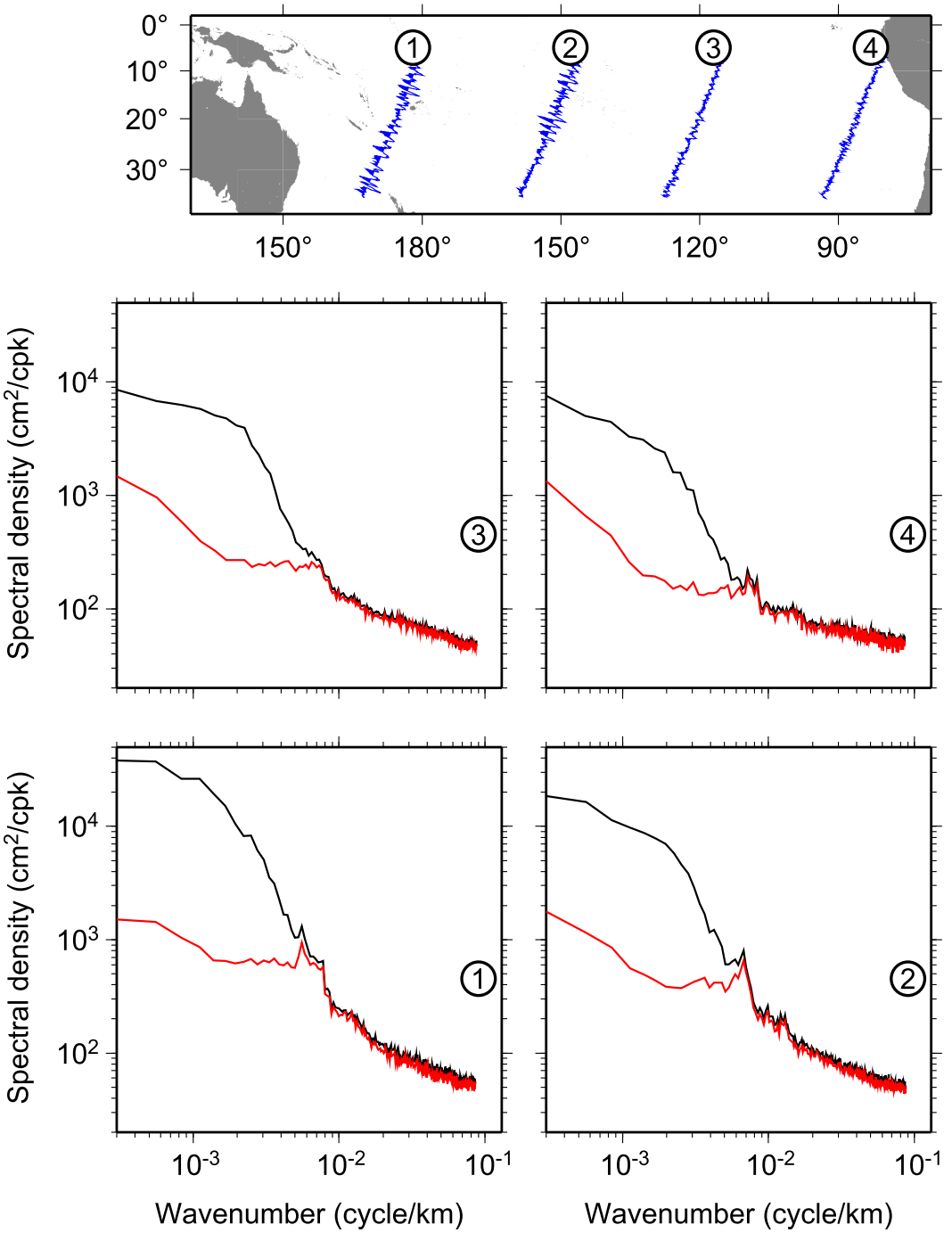

FIG. 2. Sea surface height wavenumber spectra for four T/P-J tracks crossing the South Pacific. (top) Track locations with estimated tidal amplitudes (relative scale) after high-pass along-track filtering. (bottom four) The wavenumber spectra of SSH after removal of barotropic tide (black) and after further removal of AVISO-based nontidal SSH signals (red). This mesoscale correction allows better delineation of the internal tide peaks in the 120–160-km wave band.

in the south. The northernmost internal tide signals are little affected by the mesoscale correction, although a couple of anomalies are slightly reduced in amplitude, whereas the obvious ACC variability in the south is suppressed but not completely eliminated. The midsections, especially on the *GFO* track, may be displaying better delineation of the tidal signals, but it is difficult to be certain; some anomalies appear reduced in amplitude.

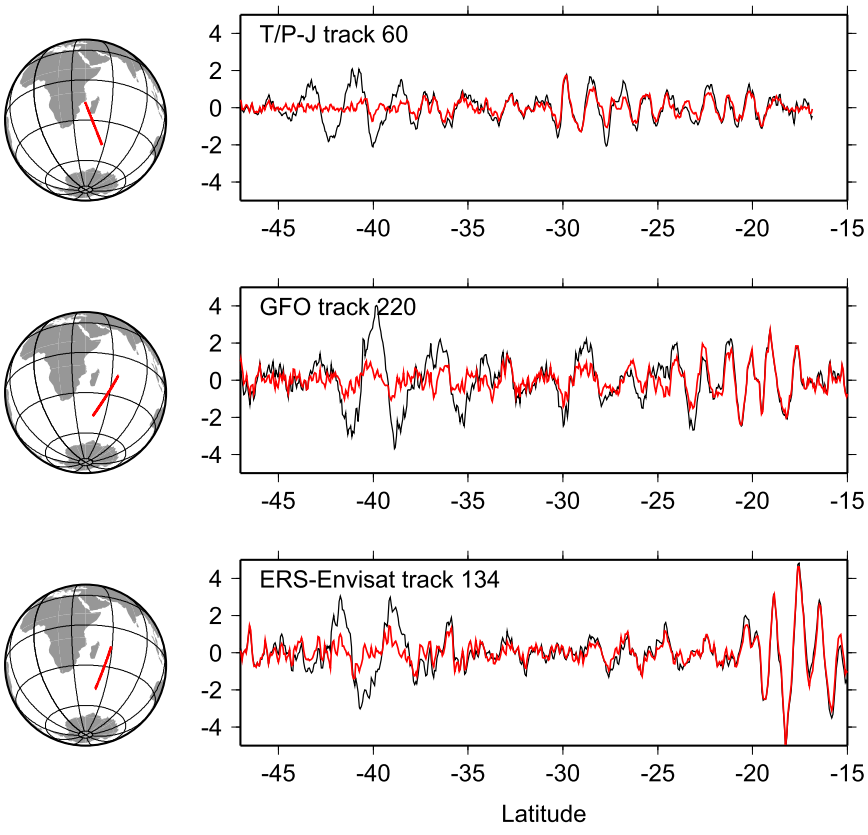

FIG. 3. Quadrature component (cm) of the M_2 tide independently estimated point-by-point along satellite tracks. Black lines are before and red lines are after correcting the altimeter data for nontidal variability, based on using two-dimensional mapped SSH data from AVISO as a prior correction. Three examples are from three different satellite missions with different tidal alias periods. For each track the signals in the north are predominantly from internal tides; the signals in the south are predominantly from mesoscale variability of the ACC.

In fact, and as noted previously (Ray and Byrne 2010), it is possible for the mesoscale correction technique to degrade tidal estimates. If tide modeling errors, or internal tide signals, have leaked into the AVISO gridded SSH data, then the correction would remove our signal. Several features of the AVISO gridding algorithms (e.g., Le Traon et al. 2003; Pascual et al. 2006; Chelton et al. 2011) act to diminish such leakage; for example, the use of as many as four different altimeters with different tidal alias periods, the relatively long (compared with tides) time correlation periods in their objective analysis, and the use of spatial covariance functions with built-in propagation speeds comparable to theoretical values for long baroclinic Rossby waves, all act to mitigate tidal leakage. Nevertheless, there is evidence for a small amount of tide error leakage into the AVISO data (see the appendix). The leakage is somewhat worse in the 2014 DUACS product, as opposed to the 2010 product, which is why we here use the latter (which covers the time period 1992–2013). Leaked internal tide signals in AVISO data are unlikely to affect any nontidal altimeter applications because the signal is so small and localized to a relatively small frequency–wavenumber band.

Perhaps the best test of whether this mesoscale correction in its present form is advantageous or not is to examine the consistency of tidal estimates at intersecting tracks. This is done in Table 2 where the discrepancies of estimated tides at cross-over locations are summarized for two ocean regions surrounding the Hawaiian Ridge and the Agulhas retroflection south of Africa. The first region is one of relatively strong internal tide signals and fairly low nontidal noise; the second is the opposite: weak tides and very high mesoscale variability. The mean along-track tidal estimation error $\langle\sigma\rangle$ in the table reflects both the number of data entering into each estimation (maximum is given by the number of repeat cycles listed in Table 1), which favors the T/P-J data, and also the background noise, which is much inflated in the Agulhas region. The background

TABLE 2. RMS differences (cm) of M_2 tidal estimates at track cross overs. RMS differences computed from in-phase and quadrature tidal components. Before/after refers to before/after correction for mesoscale variability. The $\langle\sigma\rangle$ is the tidal estimation standard error (cm) for the full tidal signal—barotropic plus baroclinic—averaged over all cross overs. The Hawaii region covers 15°–35°N, 180°E–150°W; the Agulhas region covers 45°–35°S, 10°–45°E.

Satellite mission	Number of x overs	$\langle\sigma\rangle$ before	$\langle\sigma\rangle$ after	RMS before	RMS after	RMS after + filter
			Hawaiian Ridge region			
T/P-J	73	0.50	0.24	0.56	0.40	0.38
T/P-J interlaced	74	0.80	0.40	0.86	0.59	0.51
GFO	260	1.13	0.59	2.14	0.89	0.59
ERS-*Envisat*	585	1.66	0.95	1.30	0.98	0.60
			Agulhas region			
T/P-J	60	1.19	0.41	2.70	0.55	0.36
T/P-J interlaced	60	1.87	0.68	4.21	0.83	0.64
GFO	213	2.67	1.01	6.57	2.19	0.94
ERS–*Envisat*	432	3.66	1.30	6.11	5.39	0.83

noise is naturally reduced after application of the AVISO correction, with $\langle\sigma\rangle$ often reduced by half or more. The cross-over differences show a similar pattern, with RMS differences clearly benefiting from the AVISO correction. The ERS–*Envisat* cross-over differences in the Agulhas region, however, remain abnormally high even after this correction. The estimates evidently contain significant long-wavelength errors (next section).

b. *High-pass filtering*

Even a cursory examination of the mesoscale-corrected along-track tidal estimates reveals cases of small biases or long-wavelength (>500 km) offsets, leading to inconsistencies among neighboring tracks and to cross-over discrepancies. Figure 4 (left panel) shows examples from analysis of T/P-J data over the central North Pacific. The offsets are very small—well less than 1 cm in this figure—but large enough to spoil attempts to map the small internal tide. Tidal estimates from ERS–*Envisat* and *GFO* are generally worse in this regard (also reflected in Table 2, column 6, by the high cross-over RMS values). Such inconsistencies at cross overs have been emphasized by Dushaw (2002), leading him to adopt the frequency–wavenumber filtering and mapping approach that relies on knowledge of ocean stratification, but our goal here is to avoid that, for better or worse.

The long-wavelength errors shown in Fig. 4 are not related to errors in the barotropic tidal model or to tidally coherent errors in the satellite ephemerides because such errors would be similar among neighboring passes. Rather they must be caused by other small errors; there are any number of candidates: errors in the atmospheric loading adjustments, small random errors in satellite ephemerides, errors in range delay corrections, and so on, all of which are broadband but potentially nonzero at the aliased tidal frequencies. Improvements incorporated into altimeter data reprocessing projects do address all these errors, but the errors here are so small that they will be difficult to eliminate completely.

We have experimented with a polynomial cross-over adjustment method, much like schemes used in early days of satellite altimetry to correct for orbit error (e.g., Rapp 1983; Le Traon et al. 1991), but the results were deemed unsatisfactory, still leaving too many small offsets between tracks. We have therefore applied an along-track high-pass filter to the along-track tidal estimates, similar to that used originally to separate the barotropic and baroclinic tides (Ray and Mitchum 1996). The adopted filter's wavenumber response is shown in Fig. 5. The resulting consistency among neighboring tracks is much improved—see Fig. 4 (right panel) and also Table 2 (final column).

There are, however, serious drawbacks to along-track filtering that are obvious if one considers a track running parallel to the long crest or trough of a plane wave, where the internal tide would appear long wavelength and thus removed by the filter. Figure 6 shows an example for a simple plane wave, of wavelength 140 km (typical of mode-1 M_2 waves), which is sampled with the real altimeter track pattern obtained from our four missions and then gridded using the algorithm described below in section 3. For northward- or southward-propagating plane waves, the high-pass filter causes little degradation of the signal; for eastward- or westward-propagating waves, the degradation is serious.

Using the same altimeter track pattern as in Fig. 6, Fig. 7 shows the complete filter response as a function of wave direction for three different filter cutoffs and for the same 140-km plane wave used above. For plane waves propagating within ±40°–50° of north–south, there is little signal degradation. However, for certain directions near east–west, the signal variance can be reduced by 50%–80%, depending on the cutoff wavelength.

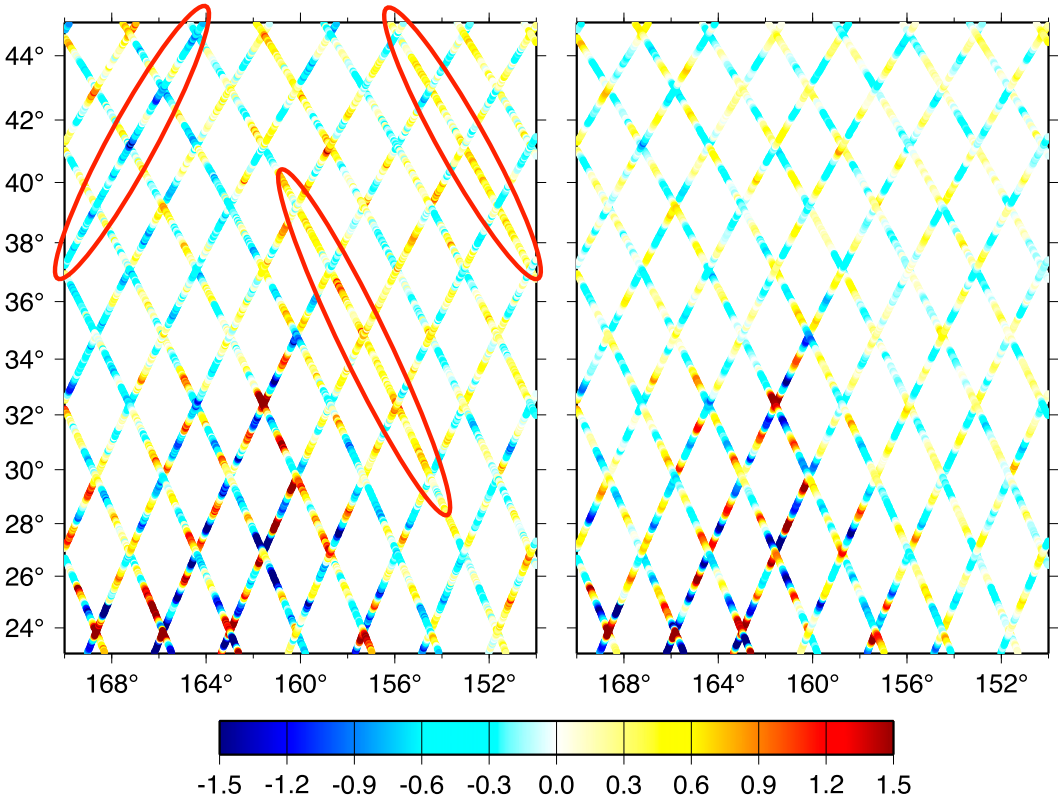

FIG. 4. Color-coded along-track tidal estimates (in-phase component, cm) for T/P-J tracks in the North Pacific (left) before and (right) after application of the along-track high-pass filter. Barotropic tide has been removed via a model. The left panel displays several tracks (e.g., those highlighted by red ellipses) seen to be biased positive or negative, leading to discrepancies with intersecting tracks. Tracks in the right panel, after filtering, are more consistent. Table 2 indicates that along-track filtering is more critical for *GFO* and ERS–*Envisat* data, although even T/P-J data benefit, as shown here.

Not surprisingly, the shortest cutoff is the worst in terms of removing real signal.

As we have become more familiar with the SSH signatures of internal tides in the real global ocean (e.g., Rainville et al. 2010; Dushaw et al. 2011; Zhao et al. 2012) or in numerical models of the ocean (e.g., Shriver et al. 2012), it must be acknowledged there are few cases of long-crested plane waves of the sort depicted in Fig. 6. Complex interference patterns from multitudes of generation sites in the real ocean tend to break apart such long-crested patterns (e.g., Rainville et al. 2010). For our purposes this is fortunate. Nonetheless, even short-crested east–west waves may possibly be degraded by the along-track filtering.

Note that Zhao et al. (2012) also employ along-track filtering, so similar degradation must result in their along-track estimates. However, it is possible that their subsequent plane wave fitting to the filtered along-track data can recover some of the lost signal.

Aside from these difficulties the along-track filtering appears more beneficial than harmful. In particular, Table 2 shows that without filtering some of the altimeter data would have errors that totally overwhelm the small signals of internal tides. Table 2 also emphasizes the disadvantages of *GFO* and ERS–*Envisat* data for along-track tidal analyses; both are evidently handicapped by the fewer number of repeat-cycle observations in an analysis and the longer M_2 tidal alias periods (especially *GFO*, whose 317-day alias is uncomfortably close to the annual cycle). The different statistics for T/P-J and its interleaved extended mission(s) give an indication of the dependence on the number of observations, since those alias periods are identical; almost 3 times more data yield a roughly 40% reduction in RMS cross-over differences.

The increased noise levels in *GFO*, in part from the nearness of the M_2 alias to the annual cycle, was noted by Zhao et al. (2011), who reported that *GFO* amplitudes were systematically larger than T/P amplitudes. Our estimates are consistent with that; see Fig. 8, where initial *GFO* amplitudes are biased high by almost 40%. However, after the mesoscale correction and the high-pass

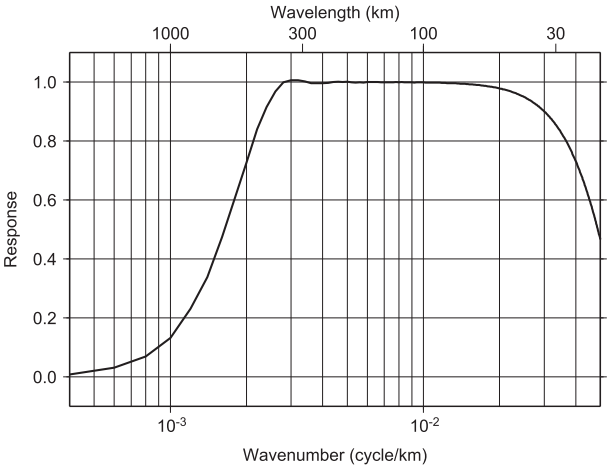

FIG. 5. Frequency response of along-track filter used to suppress small long-wavelength altimetric errors and biases as seen in Fig. 4. The filter is a finite impulse response convolution filter with nominal wavelength cutoff at 600 km. At high wavenumbers a 5-point Savitzky–Golay filter is used to suppress noise.

filter, this is reduced to 13%. The correlations also are considerably improved, from 0.26 to 0.73.

3. Empirical map of M_2

The altimetric tide estimates described above may be mapped to a regular two-dimensional grid by any number of methods, including optimal methods based on various statistical assumptions. In the initial exercises reported here, we have employed a simple and fast weighted-averaging method, the weighting based on the along-track tidal standard errors (thus generally favoring T/P-J data), with *e*-folding scales of approximately 4 km in latitude and 6 km in longitude at the equator but reducing with latitude to reflect convergence of satellite ground tracks in higher latitudes. The grid interval used is 0.05°. Ocean regions shallower than 100 m, as well as most inland and marginal seas, have been removed from the analysis, since the focus here is open-ocean internal tides.

The performance of the gridding algorithm can be partly assessed in the ''zoom view'' of Fig. 9, a small oceanic region in the tropical North Atlantic just south of Cape Verde, which is a strong generation site for the waves. The gridded result is seen to capture fairly well the along-track anomalies. Some instances of small discrepancies at track intersections are seen to be handled as well as can be expected. For example, a strong positive anomaly at 10°N, 25°W is seen to be reduced to be more consistent with the higher-weighted T/P anomaly along an intersecting track (the T/P tracks are recognizable as those with lower inclination). The large diamond-shaped gap at 10°N, 27.5°W is interpolated across smoothly in a fashion consistent with the available neighboring data. One fault might be that the peak of strong, sharp positive anomaly at 12.5°N, 27.5°W has been slightly reduced. The positive anomaly at 9.2°N, 28.5°W at first glance looks also reduced, but in fact it matches the lower amplitude seen on the one intersecting T/P track in that cluster of tracks.

Figure 10 presents a low-resolution view of the global M_2 amplitudes. Higher-resolution maps of the in-phase components, which more clearly delineate wave structures and local wavelengths, are available in Fig. S1. The high-resolution map shows the near-ubiquity of the stationary internal tide throughout the globe, in many places with amplitudes below 5 mm. Both maps mark out regions of intense generation and show long-range propagation, often confined to narrow channels (cf. Arbic et al. 2010; Rainville et al. 2010; Dushaw et al. 2011; Zhao et al. 2012).

Note that some of the high-amplitude regions near the coastlines that are apparent in Fig. 10 likely stem from errors in the barotropic model (Stammer et al. 2014); examples include the Florida Strait, the southern tip of Korea, offshore Guinea, and parts of the Aleutian chain, although several points along the Aleutians are also known to be strong generation sites (Cummins et al. 2001). One might expect that the high amplitudes within the Indonesian seas are also some combination of barotropic model errors and real baroclinic tides, but examination of Fig. S1 suggests they are mostly baroclinic, with wave patterns characteristic of the open-ocean internal tides.

Manifestly not characteristic of open-ocean internal tide patterns are our solutions in the vicinity of strong boundary currents, where the dominant pattern is noiselike; see especially Fig. S1 in the vicinity of the Agulhas retroflection. Parts of the Gulf Stream extension also likely represent mesoscale contamination, although there is also real signal there, reflecting generation near Georges Bank and the coastline of Nova Scotia. Amplitudes are very weak in the western North Atlantic above about 45°N, throughout the southern Indian below 40°S, and in the western South Atlantic below 40°S; in these regions the stationary part of M_2 appears to be below the current limits of altimetry.

Before further discussion and analysis of these empirical maps, it is worthwhile addressing in more detail their validity.

4. Tests against independent altimeter data

As a further assessment of the empirical mapping results, we used them to compute new internal tide

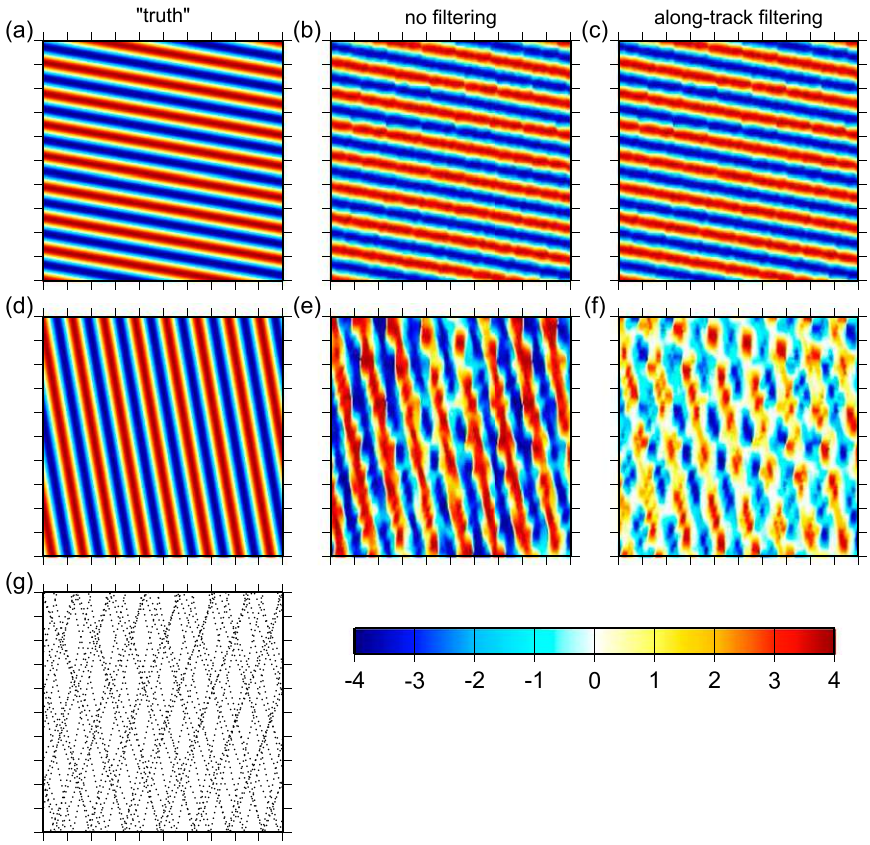

FIG. 6. Effect of along-track filtering on simulated plane waves. (a),(d) "True" wave signals, which are (g) sampled along a real pattern of satellite tracks, a $10° \times 10°$ region with lower boundary at the equator. (b),(e) After gridding sampled data but without prior filtering. (c), (f) After gridding sampled data, with prior application of along-track high-pass filter. Waves propagating north–south are properly recovered; waves propagating east–west are degraded and distorted, especially after filtering.

"corrections" for independent satellite altimeter data, the goal being to assess whether such corrections have a positive impact on residual SSH variance. In fact, future wide-swath altimeter missions, devoted to mapping the oceanic submesoscale (Fu and Ferrari 2008), will require such corrections for internal tides. Moreover, the appendix suggests that present-day altimetry may even benefit.

For these tests we used independent altimeter data from the *Cryosphere Satellite-2 (CryoSat-2)* and the *Satellite with Argos and Altika* (*SARAL*) *Ka-Band Altimeter Radiometer* (*AltiKa*) missions, as well as the extended *Jason-1* mission after the satellite was placed into a geodetic, nonrepeating orbit. The *SARAL* data do not present a particularly demanding test since that satellite flies along the same ground track as *Envisat* (although at a different local time). The *SARAL* data, nonetheless, are still independent, since they were not used in the tidal solutions. Similarly, for the *Jason-1* satellite the new tidal alias periods after the orbit shift (disregarding the lack of exact repeat) are nearly identical to those before the shift, since the *Jason-1* orbit plane precession rate was not affected, but the new data allow testing of predictions at new locations between the older tracks, which is extremely useful. *Cryosat-2* data represent perhaps the most challenging test, since it follows new ground tracks with unique tidal aliasing.

The *Cryosat-2*, *SARAL*, and *Jason-1* geodetic data cover the periods 2010–14, 2013/14, and 2012/13, respectively. Owing to their (essentially) nonrepeating orbits, the Cryosat and Jason missions rely critically on sufficiently accurate prior knowledge of the mean sea surface; for this application we used the DTU10 mean sea surface, an update to work described by Andersen and Knudsen (2009). Cryosat is also hampered by lack of onboard instruments for supplying ionospheric and wet tropospheric corrections, thus requiring model-based corrections be used instead. Dibarboure et al. (2012)

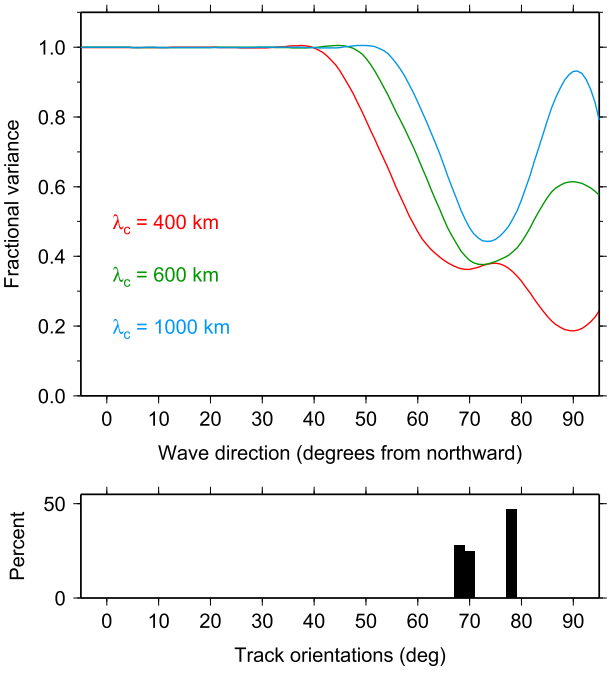

FIG. 7. Recovered variance of the plane wave of Fig. 6 after application of an along-track high-pass filter, as a function of wave direction and filter cutoff wavelength λ_c. As in Fig. 6, waves propagating in the east–west direction are poorly recovered after along-track filtering. The bottom panel is a histogram of the track orientations shown in Fig. 6g; these directions align with the reduction in variance of the top panel. Whether the variance at 90° is a local minimum or maximum seems to depend on subtle tradeoffs among the cutoff wavelength, the average track separations, and details of the gridding algorithm.

review the advantages and disadvantages of using *Cryosat-2* in oceanographic applications. To suppress nontidal variability, we employed (as above) the AVISO gridded SSH fields as a prior correction.

Figure 11 shows the residual SSH variances after applying this new internal tide correction. Residuals in all panels were averaged into 1° bins before plotting. For the most part the figure shows good reduction in variance, with open-ocean sites of internal tide generation displaying the largest reductions. Throughout the remainder of the oceans the reductions are small but usually positive. The notable exceptions are regions of high mesoscale variability, which confirms that the internal tide solutions have been corrupted by that variability, notwithstanding the use of the AVISO data as a prior correction. (Without such correction, the blue regions of Fig. 11 would be far more extensive.)

In terms of reduction of variance, the correction appears most useful for Cryosat, which is surprising in light of its differing alias periods, its (essentially) nonrepeating ground tracks, and the overall challenges of using those data for oceanographic applications (Dibarboure et al. 2012).

These results with independent data, and especially the results for Cryosat, confirm the overall validity of the internal tide solutions and suggest that new internal tide corrections are indeed feasible, at least for this stationary M_2 component and away from boundary current regions.

5. Two-dimensional wavenumber analysis of internal tide

One of the advantages of using an empirical methodology independent of theoretical properties of wave dynamics—independent even of knowledge of the mean ocean stratification—is that the results may legitimately be used to test such properties. In this section our mapped internal tide fields are subjected to two-dimensional spectral analysis with several goals in mind: to learn about the global wavenumber properties of the M_2 tide; to compare at regional resolution these properties with simple theoretical predictions for mode-1 waves; and to determine what ocean regions have detectable coherent mode-2 waves.

We treat the tidal elevation fields as complex numbers with components in phase and in quadrature with the astronomical potential at Greenwich. A two-dimensional wavenumber spectrum was successively applied to small ocean subareas spanning 20° in latitude and 20° × secφ in longitude, where φ is latitude, thus yielding local Cartesian coordinates approximately the same size in each direction. This procedure yields a spectral density $S_{hh}(k_x, k_y)$, a function of wavenumbers k_x, k_y that are both positive and negative. A Hamming window in each direction was used to reduce spectral leakage, which necessarily upweights information in the center of the region.

A selection of these two-dimensional spectra is shown in Figs. 12–15, which illustrate several noteworthy features. Figure 12, covering a region north of the Hawaiian Ridge, shows a clear circular pattern of radius $\sqrt{(k_x^2 + k_y^2)}$ approximately 0.006 cycles per kilometer (cpk), or 160-km wavelength, with energy propagating primarily to the north (and also northeast) and somewhat less so toward the south. This is consistent with waves propagating into this region from two known major generation sites at the Hawaiian Ridge and Aleutian Arc (e.g., Ray and Cartwright 2001; Zhao et al. 2011). Also apparent in the figure is a subtle secondary semicircle, mostly on the side with positive k_y, evidently representing the second baroclinic mode. Its appearance is clearer in the azimuthal integral of the 2D spectrum (inset diagram)

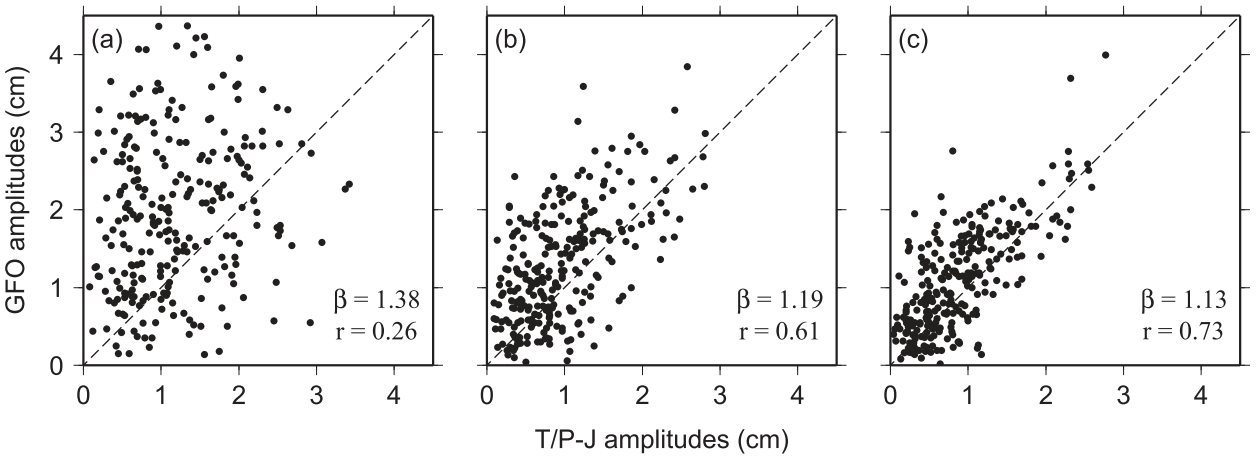

FIG. 8. Cross-over comparisons of estimated M_2 amplitudes from *GFO* vs T/P-J for a region of the North Pacific Ocean (cf. Fig. 5i of Zhao et al. 2011). Panels are (a) standard tidal estimates after removal of barotropic model, (b) after additional prior correction for nontidal variability based on gridded AVISO data, and (c) after additional along-track high-pass filtering. Parameter β is slope, determined by ordinary least squares, of a straight-line fit with zero intercept, thus describing the amount by which *GFO* amplitudes are biased high. The variable r is Pearson's correlation coefficient.

with a peak wavelength of approximately 80 km or half the first mode.

Figure 13, from the South Pacific northeast of New Zealand, delineates a spectral pattern even more fully circular, thus indicating wave propagation in nearly all directions. If track orientation and along-track filtering is removing east–west waves, as Figs. 6–7 suggested could happen, Fig. 13 shows that east–west energy is still significant in the mapped tide. In the 2D spectrum, a second mode is again evident, mostly with negative k_y. Both modes display well-defined peaks in the azimuthal integral.

Figure 14, from the equatorial eastern Pacific where the internal tidal signals are much weaker, again shows a well-defined first mode, with propagation most strongly due north and more weakly toward the west, with almost nothing toward the east and southeast. There is hardly any suggestion in this spectrum for higher modes.

In contrast, Fig. 15, from the western Pacific, shows the strongest propagation toward the west and weakest to the north. Some of the eastward energy may be arising from Luzon Strait, a known generation region for intense waves (Alford et al. 2011; Zhao 2014), although

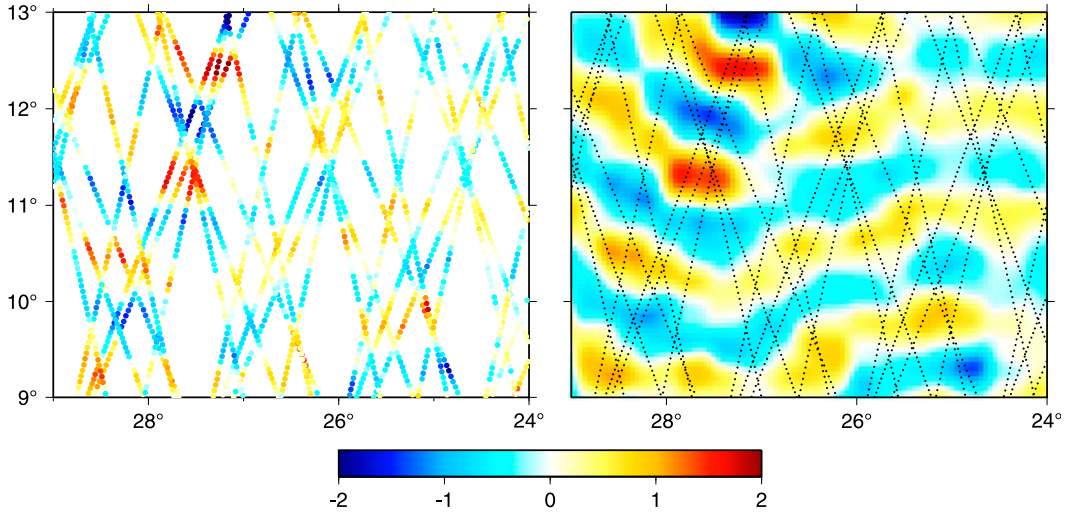

FIG. 9. A detailed view of a small area of the North Atlantic south of Cape Verde showing how the adopted gridding algorithm has turned the (left) along-track M_2 in-phase tide estimates into (right) map form. Units are cm.

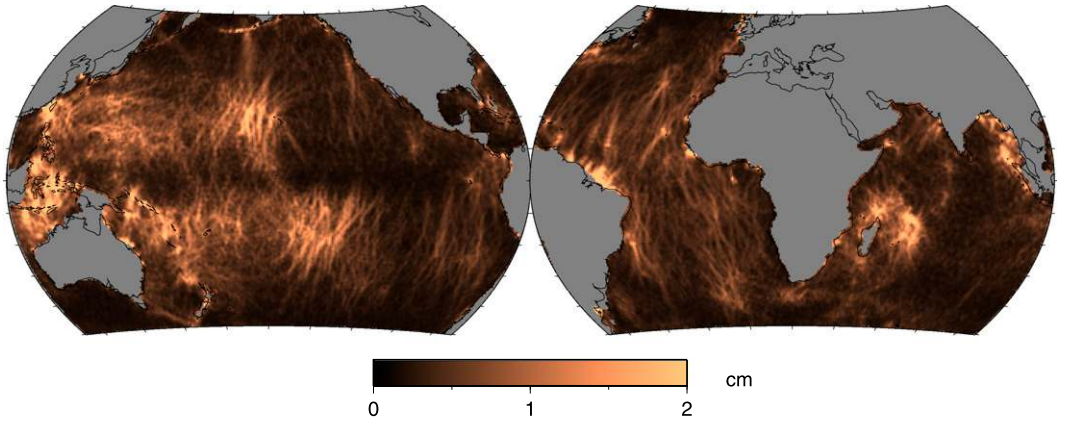

FIG. 10. Amplitudes (cm) of surface displacement of the stationary M_2 internal tide. In some places the color scale of 2 cm is exceeded. Some anomalies located along coastlines are actually unrelated to internal tides and are caused by errors in the barotropic tide model used to process the altimetry. A higher-resolution figure of the in-phase component, which is more useful for delineating waves and local wavelengths, is available as Fig. S1.

the spectrum's Hamming window necessarily down-weights signals near the edges of the analysis domain, which would include the strongest eastward energy near the western boundary of the domain. Like Fig. 14 any higher modes are not easily identified above the background noise level, but relative to our other cases there is more diffuse energy—or possibly more enhanced noise—throughout the whole wavenumber band.

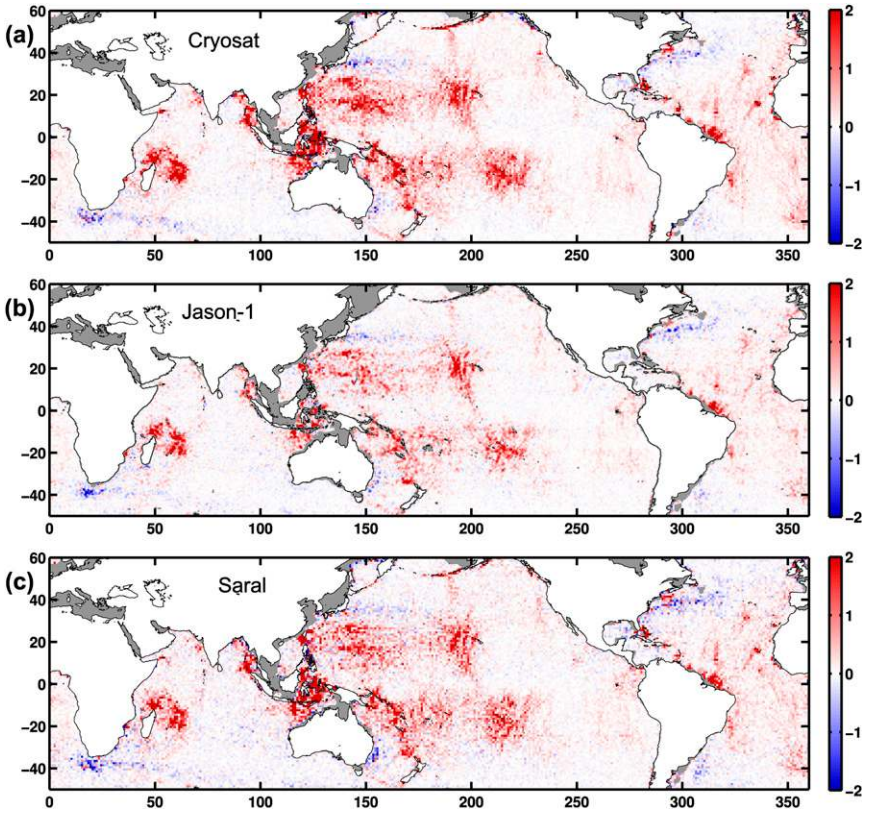

FIG. 11. Variance reduction (cm^2) when applying our empirical internal tide correction to independent altimeter measurements from (top) *Cryosat-2*, (middle) *Jason-1* geodetic mission, and (bottom) *SARAL AltiKa*. Variances are reduced in all regions of strong internal tide generation and are slightly reduced or unaffected in most other regions. Important exceptions are the blue regions where high mesoscale variability has evidently corrupted the empirical internal tide solutions.

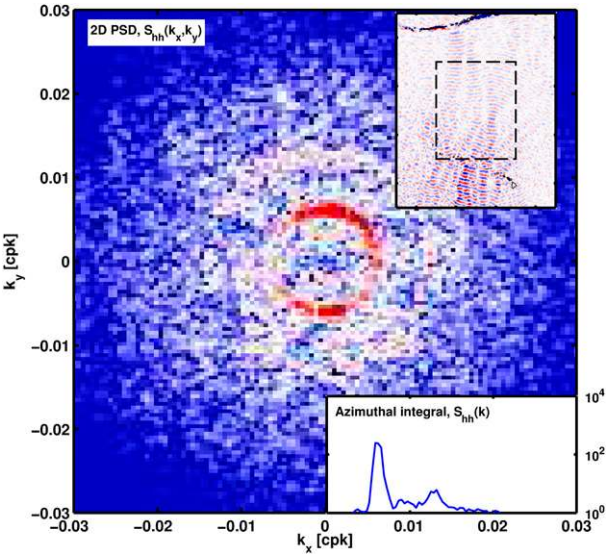

FIG. 12. Internal tide wavenumber spectrum showing strong, nearly circular pattern of energy corresponding to a wavenumber magnitude $\sqrt{(k_x^2 + k_y^2)}$ for a first baroclinic mode for the region 25°–45°N, 175°–155°W, north of the Hawaiian Ridge (inset map, top right). The azimuthal integral of the two-dimensional spectrum (inset, bottom right) shows the pronounced peak from this mode at wavelength approximately 160 km, as well as a secondary peak of a second mode at approximately 80 km.

In fact, the possibility that some of the ''background'' variance in Figs. 12–15, including that lying between the mode-1 and mode-2 wavenumber rings, might be a real signal and not simply estimation or mapping noise

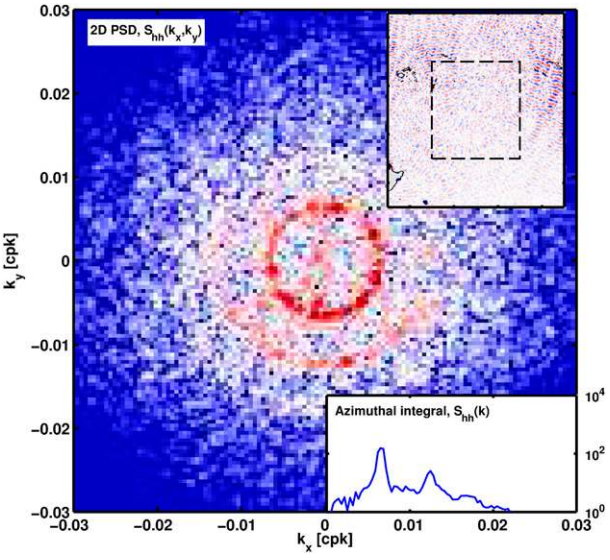

FIG. 13. As in Fig. 12, but for the region 35°–15°S, 180°–160°W, northeast of New Zealand. First mode displays propagation in all directions; second mode is also evident, primarily toward the south.

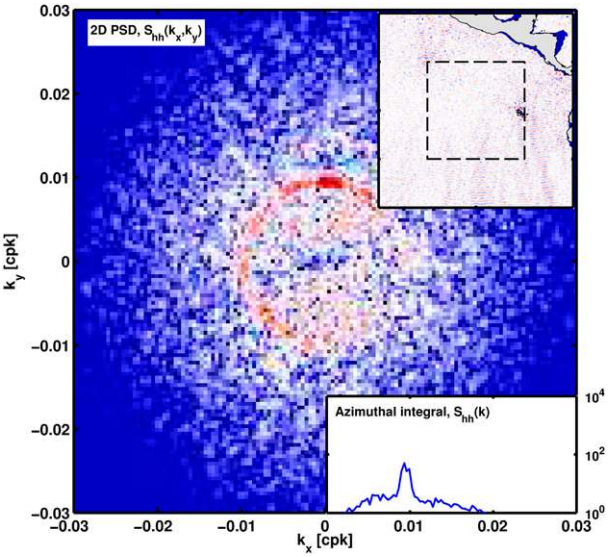

FIG. 14. As in Fig. 12, but for the region 10°S–10°N, 110°–90°W, in the eastern Pacific.

should not be casually dismissed. For example, it is conceivable that some variance could be associated with topographic scattering of evanescent waves whose wavenumbers are set directly by the topographic forcing rather than the dispersion relation. Identification of possible real signals that lie off the dispersion relation

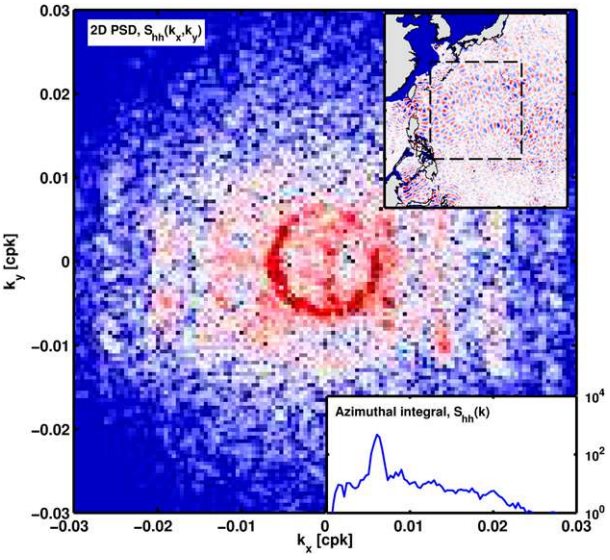

FIG. 15. As in Fig. 12, but for the region 10°–30°N, 125°–145°E, in the western Pacific. This region is affected by waves from a large number of known generation sites, and the spectrum thus reflects wave propagation in most directions, although somewhat weaker toward the north and northeast. Waves from Luzon Strait may be partially concealed by the cosine windowing used for spectral analysis.

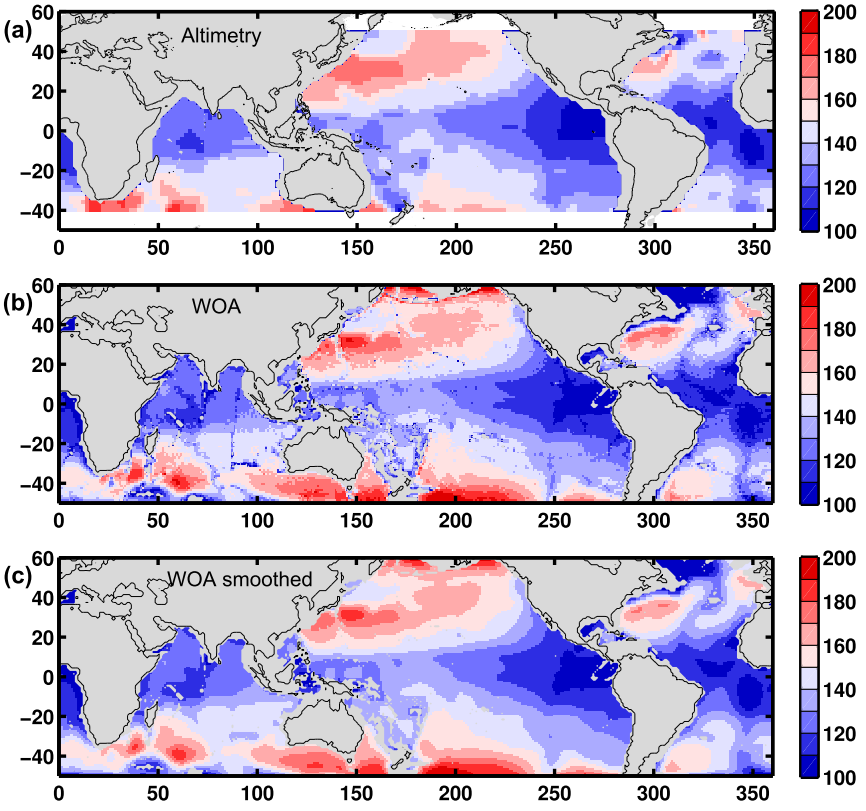

FIG. 16. Wavelengths (km) of the M_2 first baroclinic mode. (top) As deduced from two-dimensional spectra of the empirical M_2 global chart derived from satellite altimetry. (middle) As calculated by solving the Sturm–Liouville eigenvalue problem for the vertical structure function, with the mean annual ocean stratification defined by the *World Ocean Atlas*. (bottom) As in the middle, but after smoothing with a 1000-km window. The effective resolution of the top panel is also roughly 1000 km, since it is based on spectral estimates from ~20° × 20° ocean regions (cf. Fig. 12).

could yield new insights into the tidal dynamics. The matter warrants further investigation.

Returning to the dominant spectral energy evident in the figures, we find the first modal peak in the azimuthal spectra is nearly always identifiable. Thus, the locations of those peaks may be used to map globally the first-mode wavelength, at least at the regional resolution corresponding to our 2D spectra. The result is Fig. 16a. The mapped wavelengths appear quite reasonable, ranging from 100 km in the western equatorial Pacific and Atlantic to somewhat more than 170 km. The longest wavelengths, however, tend to coincide with regions where the underlying empirical tide estimates are less reliable (and indeed in regions where the variance tests of Fig. 11 suggest little predictive skill), so those areas must be accepted with some caution.

Nonetheless, we find the agreement with theoretically predicted wavelengths remarkably good. For such comparison, the wavelengths of the mode-1 M_2 internal tide have been computed from vertical profiles of buoyancy frequency that are based on the annual average ocean temperature and salinity profiles in the *World Ocean Atlas* (*WOA*; Locarnini et al. 2010; Antonov et al. 2010). The mode-1 wavelengths were computed by solving the locally defined Sturm–Liouville problem for the vertical modes, assuming flat-bottom topography and neglecting advection and shear of the background flow (Gill 1982). Figure 16b illustrates the result of this calculation. As in Fig. 16a the main features evident are the contrast between the shorter wavelengths in the equatorial zones and the longer wavelengths in midlatitudes. The influence of bottom depth is also apparent at the mid-Atlantic Ridge, the Mariana Plate, and elsewhere.

Because the altimeter-determined wavelengths were identified from the wavenumber spectra, their values are representative of the average wavelength over the windows used to compute the spectra, which is about 1000 km. Thus, for better comparison between the empirical and theoretical mode-1 wavelengths, Fig. 16c shows the same field as Fig. 16b except smoothed over a

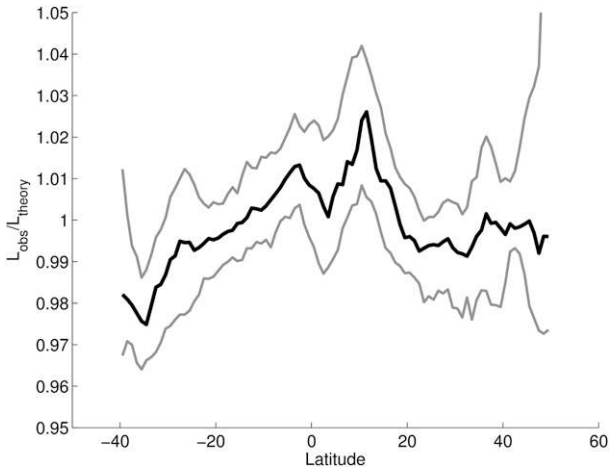

FIG. 17. Median (heavy line) of the ratio of observed vs theoretical mode-1 wavelengths, according to Figs. 16a and 16c, as function of latitude. Upper and lower quartiles are indicated in gray.

1000-km window. The features, which are now somewhat blurred, may be compared with the empirically estimated wavelengths in Fig. 16a. The two fields, the global average values of which agree to within 0.2%, show many of the same features, including the main latitudinal variations and differences between the Atlantic, Pacific, and Indian Oceans. Even the relatively small-scale features related to topography are present, albeit somewhat attenuated, in the empirical map. A couple of noteworthy differences between Figs. 16a and 16c include the Tasman Sea (northwest of New Zealand) and the South Pacific extending westward from Chile.

Figure 17 displays the ratio of the zonal average empirical-to-theoretical mode-1 wavelengths. Systematic differences between the fields do exist—for example, the almost 3% discrepancy near 10°N—but these may be an artifact of the spatial averaging. It is apparent that the differences between the theoretical and observed wave properties are far smaller than what was found in the study of baroclinic Rossby waves from altimetry (e.g., Tailleux and McWilliams 2001). Determining the significance of the present differences would require higher spatial resolution mapping of the mode-1 wavelength, but there is a trade-off between resolution and accuracy since the wavelength is estimated from the power spectrum. Overall, it appears that the deviation between the empirical and theoretical wavelengths is smaller than would be expected from a previous estimate of Doppler effects and sheared background flow (Zaron and Egbert 2014).

Li et al. (2015) have recently performed a similar exercise, comparing theoretical mode-1 wavelengths with those computed from a tidal analysis of the STORM-TIDE simulation, which is a global 0.1° general circulation model forced by both momentum and buoyancy fluxes and the astronomical tidal potential (Müller et al. 2012). They also investigate in some detail the interplay between variations in the Coriolis parameter and variations in the mean buoyancy frequency for determining the spatial patterns evident in Fig. 16. Their simulated wavelengths are overall in good agreement with ours,

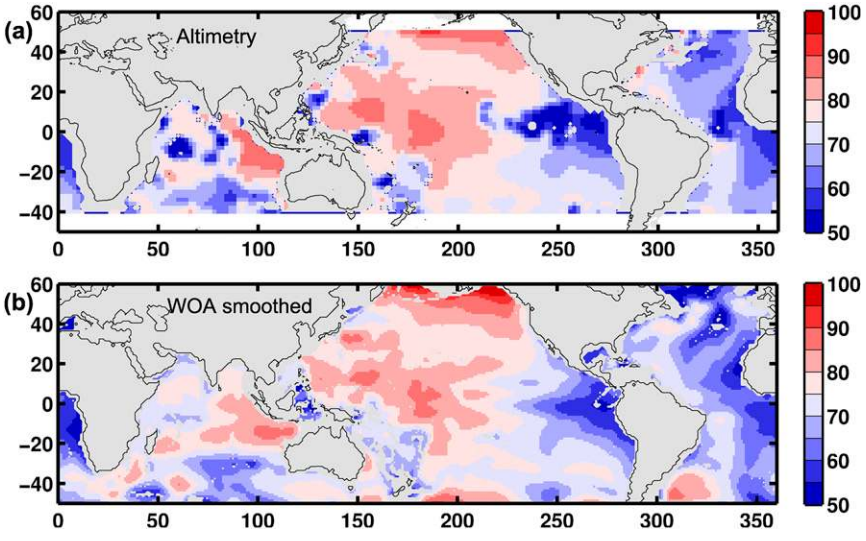

FIG. 18. Wavelength (km) of the M_2 second baroclinic mode. (top) Empirical estimates from altimetry, deduced from the two-dimensional spectra. Gray shading indicates signal-to-noise of mode-2 spectral amplitude less than 1.5. (bottom) Theoretical estimates based on stratification from the *World Ocean Atlas* (smoothed as in Fig. 16c).

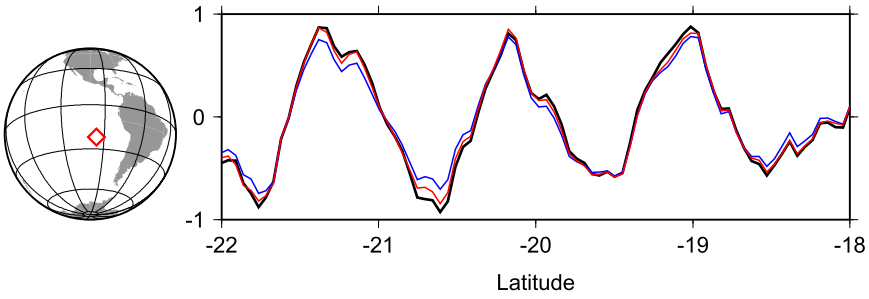

FIG. A1. Quadrature component (cm) of the high-pass filtered M_2 tide for a short segment of T/P-J pass 63 in a region of quiescent mesoscale variability. Black curve is without correcting for nontidal variability; red curve employs a correction based on AVISO DUACS 2010 SSH data; blue curve is based on DUACS 2014 SSH data. If nontidal variability is truly minimal along this track, then it is desirable for all curves to overlap. The 2014-based correction (blue curve) appears to remove more of the true tidal signal.

although there are differences in details, as must be expected.

Finally, as is evident in several of the 2D spectra, the mode-2 wave is detectable in many places. Figure 18 compares the mode-2 wavelength inferred from altimetry with the same quantity calculated from *WOA* stratification. Throughout much of the Pacific and eastern Atlantic the signal is fairly robust and in very good agreement with theoretical expectations. Signal-to-noise is considerably lower for mode 2 than for mode 1, and short mode-2 wavelength estimates are associated in some places with very weak signals. An example is the central Indian Ocean, where there are evident differences between the two maps. It is likely that at these very short (<60 km) wavelengths our adopted mesoscale correction is of little benefit (cf. Fig. A3). More importantly, however, the relatively sparse tracks of the current altimeter constellation limits satisfactory empirical mapping at such short scales.

6. Summary

This work represents an attempt to map the near-global M_2 internal tide field using a strictly empirical analysis of satellite altimeter data with no reliance on knowledge of wave dynamics or ocean stratification. There are advantages and disadvantages to such an approach. One advantage is that the results are independent of dynamical assumptions and indeed can be used to test such assumptions, as Figs. 16 and 18 show. An important disadvantage is that, owing to limitations of present-day altimetry (spatial coverage, track orientation, systematic errors, and so on), the resulting maps may be less accurate than they might be when using ocean dynamics in some way, either by exploiting theoretical wave dispersion relationships (Dushaw et al. 2011) or by employing a full numerical ocean model with formal data assimilation (Egbert and Erofeeva 2014).

Despite its possible limitations we consider an empirical approach attractive for what it reveals from the satellite data alone and also for preparing for future work with new satellite data. This initial study can be improved in many ways, including more sophisticated mapping methods and extension to other tidal constituents. Additional satellite altimeter data are anticipated in the near future, such as the European Space Agency's Sentinel-3 mission (sun-synchronous but following different ground tracks than *Envisat*; Donlon et al. 2012) and early in the next decade a wide-swath altimeter mission (Fu and Ubelmann 2014). In fact, the latter gives us considerable motivation to improve the accuracies of the mapped internal tide fields because to study submesoscale variability in the ocean, a wide-swath altimeter will require that internal tides be predicted—to the extent they can be—and removed from the data, much as current altimeter practice requires that the barotropic tide be predicted and removed. And much like current altimetry, wide-swath altimetry will also provide an invaluable new data source for mapping those same tides.

Acknowledgments. The satellite data, path delay, and other geophysical corrections used in this study were extracted from the Radar Altimeter Database System (Schrama et al. 2000; Scharroo et al. 2013) and from an augmented version of the Integrated Multi-Mission Ocean Altimeter Database (http://podaac.jpl.nasa.gov/dataset/MERGED_TP_J1_OSTM_OST_ALL_V2). The AVISO gridded altimetric data were produced by Ssalto/DUACS with support from the Centre National d'Etudes Spatiales. This work was funded by the National Aeronautics and Space Administration under the Ocean Surface Topography program.

APPENDIX

Tidal Leakage in AVISO Gridded Sea Surface Heights

Before analyzing the altimeter time series for tides, it is desirable to remove as much of the nontidal signal as possible to reduce the broadband variance that contaminates estimated harmonic constants. As noted in the main text, AVISO's DT-2010 SSH maps are useful for removing such nontidal variability before the altimeter data are subjected to tidal analysis. The procedure is seen to better isolate internal tidal peaks in wavenumber spectra. It also clearly suppresses, but usually does not completely eliminate, the large nontidal "noise" from regions of high mesoscale variability (e.g., Fig. 3). As originally stressed, however, the procedure can be risky (Ray and Byrne 2010). If real tidal signals have leaked into the AVISO gridded data, then using such data as a prior correction removes part of our signal.

In fact, as documented below, such tidal leakage does occur. In near-coastal regions it is quite easy to find cases of significant leakage, generally identifiable as false variability at the tidal alias periods. But these are caused by errors in the adopted barotropic tide model. For open-ocean internal tides, which are the subject of interest here, the leakage is very small, but nonzero.

The leakage appears somewhat worse in the latest 2014 DUACS version than in the older 2010 version. The newer product employs slightly reduced correlation scales for mapping, with reduced along-track filtering (AVISO 2014). These reduced scales were shown by Capet et al. (2014) to result in improved definition of mesoscale eddies in eastern boundary upwelling regions. They also probably account for the different tide leakage properties. Updated and generally improved altimeter corrections probably are not relevant; neither product could have employed a correction for internal tides. In our altimeter processing above, we used the 2010 data.

Although the examples in Fig. 3 do show instances of slightly reduced anomalies after applying this mesoscale correction, it is difficult to assess whether that is undesirable because the tracks are in regions of large mesoscale variability. The data in Fig. A1, however, are from a region in the eastern South Pacific with unusually quiescent mesoscale activity. In this case we might expect the data to be unaffected by any correction. Although the correction based on the DUACS 2010 data does remove a small amount of energy near latitudes 21.3° and 19°S, the correction based on DUACS 2014 data removes noticeably more; the red and black curves are more consistently aligned. The internal tide itself is small along this track—amplitude less than 1 cm—and the maximum difference between proposed corrections is 1.5 mm, with an rms difference of only 0.4 mm.

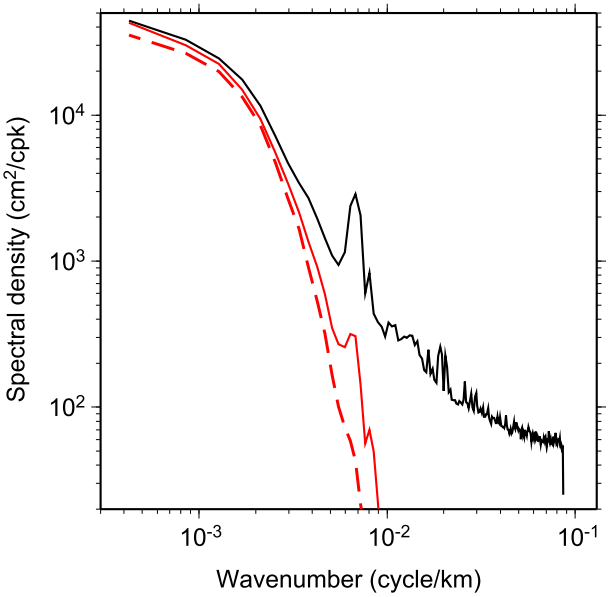

FIG. A2. Along-track wavenumber spectrum for a section of T/P-J pass 249, which extends southwest of French Frigate Shoals. Black curve is computed from the altimetric SSH after the barotropic tide has been removed. Red solid line is computed from the AVISO DUACS 2014 gridded SSH data, extracted for the identical profiles, and the red dashed line is computed from the DUACS 2010 data.

The magnitude of the contamination problem can be better illustrated by considering along-track SSH spectra in a region where the internal tide signal is relatively large. Consider T/P-J pass 249 along a section running south of the Hawaiian Ridge (from 10° to 30°N; cf. Rainville et al. 2010). Figure A2 shows the wavenumber spectra over this section, similar to those of Fig. 2, with a notable peak near 6×10^{-3} cpk associated with the internal tide. Whereas Fig. 2 showed the SSH spectra before and after removal of the AVISO-based correction, Fig. A2 shows the AVISO spectra themselves (sampled along the same repeated profiles), both the 2010 and 2014 versions. Note the peak at the same internal tide wavenumber in the 2014 spectrum and also a small, subtle shoulder in the 2010 spectrum. In other satellites passes examined, we have found the 2014 peak more or less pronounced but in all cases well above the levels of the 2010 spectra.

Figure A3 illustrates these same features in the two-dimensional wavenumber–frequency domain for the same T/P-J pass. Alias frequencies (for T/P-J sampling) of the largest tides (M_2, S_2, K_1, and O_1) are marked, as are the approximate wavenumbers of the lowest-mode M_2 and K_1 internal tides. Enhanced variance associated

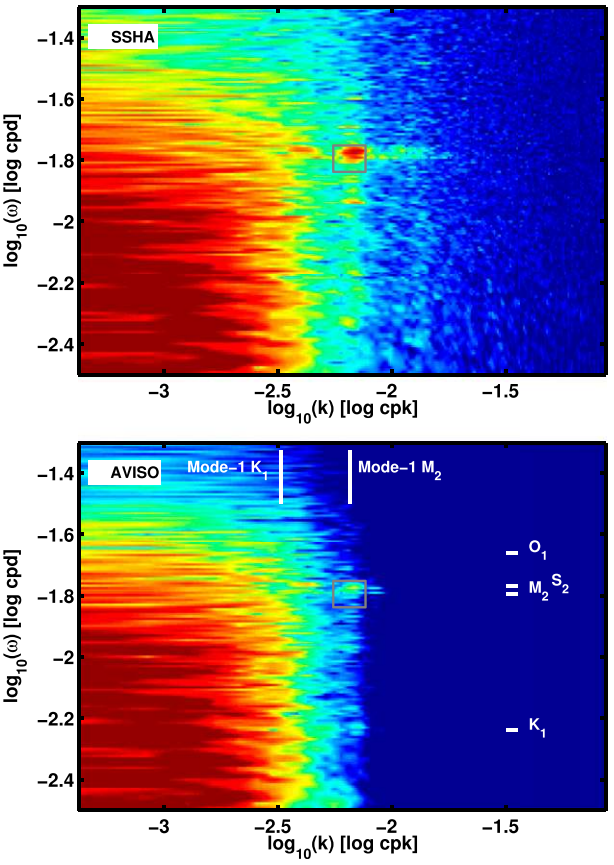

FIG. A3. Wavenumber–frequency spectra for T/P-J pass 249 data. (top) Observed along-track altimeter data after removal of barotropic tide. (bottom) AVISO DUACS 2014 data sampled along same track. The gray rectangles delimit the near-M_2 wavenumber and (aliased) frequency bands, which highlights anomalous residual energy in AVISO from internal tide leakage. The gray rectangles also delimit the bands over which the spectrum is integrated and displayed in Fig. A4.

with the mode-1 internal M_2 tide is apparent in the AVISO spectra (enclosed by gray box). The latter corresponds to the 2014 data; the residual energy for the 2010 data (not shown) is much less but is still noticeably enhanced above background.

To focus further on this tidal variance, we have integrated slices of the two-dimensional spectra across the M_2 wavenumber and frequency bands (i.e., across the gray rectangles in Fig. A3). Results are shown in Fig. A4. In this example, the M_2-band variance in the 2014 AVISO data is 0.06 cm^2, which corresponds to an internal tide amplitude of 3 mm, and which is almost one-tenth as large as the SSH variance in the same band, 0.64 cm^2. The thick line segment on the x axis indicates a frequency bandwidth of 1 yr^{-1}, centered on the M_2 alias period, which is comparable to the width of the tidal band; this is suggestive of physical tidal modulations, present in both the raw SSH as well as the AVISO

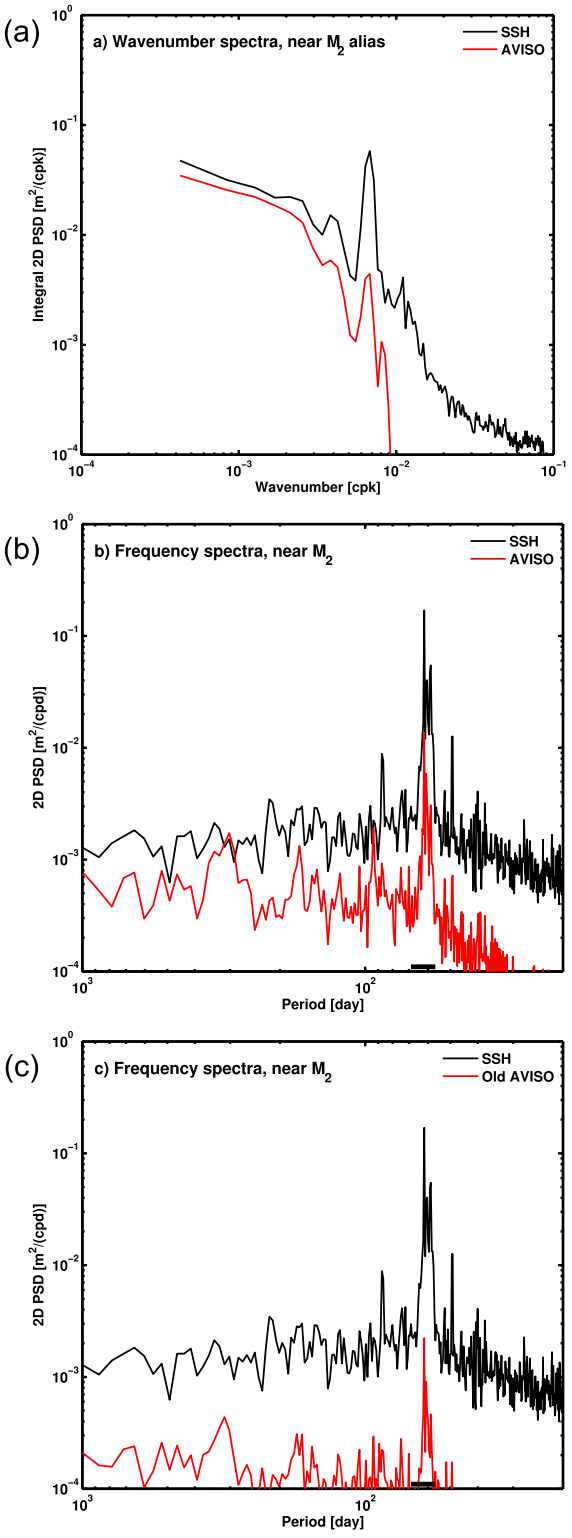

FIG. A4. Integrals across the M_2 internal tide band of the two-dimensional spectra of Fig. A3. Integration in (a) wavenumber domain and frequency domain, with black curves corresponding to the altimetric measured SSH data and red curves corresponding to the AVISO gridded SSH data from (b) 2014 and (c) 2010 DUACS versions.

product, and comparable to time scales found in this region (Colosi and Munk 2006). The M_2-band variance in the older 2010 data is only 0.01 cm^2, and it is significantly below the variance of 2014 data across the entire frequency band, which is consistent with somewhat greater spatial smoothing having been applied in the older data. While the 2010 variance is much smaller, it is still not negligible in analyses of internal tides, and it could be especially important in studies that attempt to separate stationary from nonstationary components.

We should stress that the SSH variance associated with internal tides in the gridded AVISO products is unlikely to be of any concern for most oceanographic applications. For tidal studies, however, considerable care is needed when applying this mesoscale correction to the altimeter data. We can envision an eventual iterative procedure whereby maps such as the ones we have constructed here are used to model and remove internal tide variance in AVISO's processing, which in turn will allow improved mesoscale corrections for tidal studies.

REFERENCES

Alford, M. H., and Coauthors, 2011: Energy flux and dissipation in Luzon Strait: Two tales of two ridges. *J. Phys. Oceanogr.*, **41**, 2211–2222, doi:10.1175/JPO-D-11-073.1.

Andersen, O. B., and P. Knudsen, 2009: DNSC08 mean sea surface and mean dynamic topography models. *J. Geophys. Res.*, **114**, C11001, doi:10.1029/2008JC005179.

Antonov, J. I., and Coauthors, 2010: *Salinity*. Vol. 2, *World Ocean Atlas 2009*, NOAA Atlas NESDIS 68, 184 pp.

Arbic, B. K., A. J. Wallcraft, and E. J. Metzger, 2010: Concurrent simulation of the eddying general circulation and tides in a global ocean model. *Ocean Modell.*, **32**, 175–187, doi:10.1016/j.ocemod.2010.01.007.

AVISO, 2014: A new version of SSALTO/DUACS products available in April 2014. CNES Tech. Rep., 32 pp.

Capet, A., E. Mason, V. Rossi, C. Troupin, Y. Faugère, I. Pujol, and A. Pascual, 2014: Implications of refined altimetry on estimates of mesoscale activity and eddy-driven offshore transport in the eastern boundary upwelling systems. *Geophys. Res. Lett.*, **41**, 7602–7610, doi:10.1002/2014GL061770.

Carrère, L., C. Le Provost, and F. Lyard, 2004: On the statistical stability of the M_2 barotropic and baroclinic tidal characteristics from along-track TOPEX/Poseidon satellite altimetry analysis. *J. Geophys. Res.*, **109**, C03033, doi:10.1029/2003JC001873.

Chelton, D. B., M. G. Schlax, and R. M. Samelson, 2011: Global observations of nonlinear mesoscale eddies. *Prog. Oceanogr.*, **91**, 167–216, doi:10.1016/j.pocean.2011.01.002.

Colosi, J. A., and W. Munk, 2006: Tales of the venerable Honolulu tide gauge. *J. Phys. Oceanogr.*, **36**, 967–996, doi:10.1175/JPO2876.1.

Cummins, P. F., J. Y. Cherniawsky, and M. G. G. Foreman, 2001: North Pacific internal tides from the Aleutian ridge: Altimeter observations and modeling. *J. Mar. Res.*, **59**, 167–191, doi:10.1357/002224001762882628.

Dibarboure, G., C. M.-I. Pujol, F. Briol, P.-Y. Le Traon, G. Larnicol, N. Picot, F. Mertz, and M. Ablain, 2011: *Jason-2* in DUACS: First tandem results and impact on processing and products. *Mar. Geod.*, **34**, 214–241, doi:10.1080/01490419.2011.584826.

——, C. Renaudie, M.-I. Pujol, S. Labroue, and N. Picot, 2012: A demonstration of the potential of *Cryosat-2* to contribute to mesoscale observation. *Adv. Space Res.*, **50**, 1046–1061, doi:10.1016/j.asr.2011.07.002.

Donlon, C., and Coauthors, 2012: The Global Monitoring for Environment and Security (GMES) Sentinel-3 mission. *Remote Sens. Environ.*, **120**, 37–57, doi:10.1016/j.rse.2011.07.024.

Durand, M., L.-L. Fu, D. P. Lettenmaier, D. E. Alsdorf, E. Rodriguez, and D. Esteban-Fernandez, 2010: The Surface Water and Ocean Topography mission: Observing terrestrial surface water and oceanic submesoscale eddies. *Proc. IEEE*, **98**, 766–779, doi:10.1109/JPROC.2010.2043031.

Dushaw, B. D., 2002: Mapping low-mode internal tides near Hawaii using TOPEX/POSEIDON altimeter data. *Geophys. Res. Lett.*, **29**, 1250, doi:10.1029/2001GL013944.

——, P. F. Worcester, and M. A. Dzieciuch, 2011: On the predictability of mode-1 internal tides. *Deep-Sea Res.*, **58**, 677–698, doi:10.1016/j.dsr.2011.04.002.

Egbert, G. D., and S. Y. Erofeeva, 2014: Mapping M_2 internal tides using a data-assimilative reduced gravity model. *2014 Fall Meeting*, San Francisco, CA, Amer. Geophys. Union, Abstract OS43F-01.

Fu, L.-L., and R. Ferrari, 2008: Observing oceanic submesoscale processes from space. *Eos, Trans. Amer. Geophys. Union*, **89**, 488–489, doi:10.1029/2008EO480003.

——, and C. Ubelmann, 2014: On the transition from profile altimeter to swath altimeter for observing global ocean surface topography. *J. Atmos. Oceanic Technol.*, **31**, 560–568, doi:10.1175/JTECH-D-13-00109.1.

Gill, A. E., 1982: *Atmosphere–Ocean Dynamics*. Academic Press, 662 pp.

Le Traon, P.-Y., P. Gaspar, and C. Boissier, 1991: Analysis of errors due to polynomial adjustment of altimeter profiles. *J. Atmos. Oceanic Technol.*, **8**, 385–396, doi:10.1175/1520-0426(1991)008<0385:AOEDTP>2.0.CO;2.

——, Y. Faugère, F. Hernandez, J. Dorandeau, F. Mertz, and M. Ablain, 2003: Can we merge *GEOSAT Follow-On* with TOPEX/Poseidon and *ERS-2* for an improved description of the ocean circulation? *J. Atmos. Oceanic Technol.*, **20**, 889–895, doi:10.1175/1520-0426(2003)020<0889:CWMGFW>2.0.CO;2.

Li, Z., J.-S. von Storch, and M. Müller, 2015: The M_2 internal tide simulated by a 0.1° OGCM. *J. Phys. Oceanogr.*, **45**, 3119–3135, doi:10.1175/JPO-D-14-0228.1.

Locarnini, R. A., A. V. Mishonov, J. I. Antonov, T. P. Boyer, H. E. Garcia, O. K. Baranova, M. M. Zweng, and D. R. Johnson, 2010: *Temperature*. Vol. 1, *World Ocean Atlas 2009*, NOAA Atlas NESDIS 68, 184 pp.

Müller, M., J. Y. Cherniawsky, M. G. G. Foreman, and J.-S. von Storch, 2012: Global M_2 internal tide and its seasonal variability from high resolution ocean circulation and tide modeling. *Geophys. Res. Lett.*, **39**, L19607, doi:10.1029/2012GL053320.

Niwa, Y., and T. Hibiya, 2001: Numerical study of the spatial distribution of the M_2 internal tide in the Pacific Ocean. *J. Geophys. Res.*, **106**, 22 441–22 449, doi:10.1029/2000JC000770.

——, and ——, 2004: Three-dimensional numerical simulation of the M_2 internal tides in the East China Sea. *J. Geophys. Res.*, **109**, C04027, doi:10.1029/2003JC001923.

Pascual, A., Y. Faugère, G. Larnicol, and P.-Y. Le Traon, 2006: Improved description of the ocean mesoscale variability by combining four satellite altimeters. *Geophys. Res. Lett.*, **33**, L02611, doi:10.1029/2005GL024633.

Rainville, L., T. M. S. Johnston, G. S. Carter, M. A. Merrifield, R. Pinkel, P. F. Worcester, and B. D. Dushaw, 2010: Interference pattern and propagation of the M_2 internal tide south of the Hawaiian Ridge. *J. Phys. Oceanogr.*, **40**, 311–325, doi:10.1175/2009JPO4256.1.

Rapp, R. H., 1983: The determination of geoid undulations and gravity anomalies from SEASAT altimeter data. *J. Geophys. Res.*, **88**, 1552–1562, doi:10.1029/JC088iC03p01552.

Ray, R. D., 2013: Precise comparisons of bottom-pressure and altimetric ocean tides. *J. Geophys. Res. Oceans*, **118**, 4570–4584, doi:10.1002/jgrc.20336.

——, and G. T. Mitchum, 1996: Surface manifestation of internal tides generated near Hawaii. *Geophys. Res. Lett.*, **23**, 2101–2104, doi:10.1029/96GL02050.

——, and D. E. Cartwright, 2001: Estimates of internal tide energy fluxes from Topex/Poseidon altimetry: Central North Pacific. *Geophys. Res. Lett.*, **28**, 1259–1262, doi:10.1029/2000GL012447.

——, and D. A. Byrne, 2010: Bottom pressure tides along a line in the southeast Atlantic Ocean and comparisons with satellite altimetry. *Ocean Dyn.*, **60**, 1167–1176, doi:10.1007/s10236-010-0316-0.

——, and E. D. Zaron, 2011: Non-stationary internal tides observed with satellite altimetry. *Geophys. Res. Lett.*, **38**, L17609, doi:10.1029/2011GL048617.

Scharroo, R., E. W. Leuliette, J. L. Lillibridge, D. Byrne, M. C. Naeije, and G. T. Mitchum, 2013: RADS: Consistent multimission products. *Proc. of the Symposium on 20 Years of Progress in Radar Altimetry*, Special Publication SP-710, Venice, Italy, European Space Agency, 9.

Schrama, E., R. Scharroo, and M. Naeije, 2000: Radar Altimeter Database System (RADS): Towards a generic multi-satellite altimeter database system. Delft Institute for Earth-Oriented Space Research DEOS Rep., 88 pp.

Shriver, J. F., B. K. Arbic, J. G. Richman, R. D. Ray, E. J. Metzger, A. J. Wallcraft, and P. G. Timko, 2012: An evaluation of the barotropic and internal tides in a high resolution global ocean circulation model. *J. Geophys. Res.*, **117**, C10024, doi:10.1029/2012JC008170.

Stammer, D., 1997: Global characteristics of ocean variability estimated from regional TOPEX/Poseidon altimeter measurements. *J. Phys. Oceanogr.*, **27**, 1743–1769, doi:10.1175/1520-0485(1997)027<1743:GCOOVE>2.0.CO;2.

——, and Coauthors, 2014: Accuracy assessment of global barotropic ocean tide models. *Rev. Geophys.*, **52**, 243–282, doi:10.1002/2014RG000450.

Tailleux, R., and J. C. McWilliams, 2001: The effect of bottom pressure decoupling on the speed of extratropical, baroclinic Rossby waves. *J. Phys. Oceanogr.*, **31**, 1461–1476, doi:10.1175/1520-0485(2001)031<1461:TEOBPD>2.0.CO;2.

Zaron, E. D., and G. D. Egbert, 2006: Verification studies for a z-coordinate primitive-equation model: Tidal conversion at a mid-ocean ridge. *Ocean Modell.*, **14**, 257–278, doi:10.1016/j.ocemod.2006.05.007.

——, and ——, 2014: Time-variable refraction of the internal tide at the Hawaiian Ridge. *J. Phys. Oceanogr.*, **44**, 538–557, doi:10.1175/JPO-D-12-0238.1.

Zhao, Z., 2014: Internal tide radiation from the Luzon Strait. *J. Geophys. Res. Oceans*, **119**, 5434–5448, doi:10.1002/2014JC010014.

——, M. H. Alford, J. A. MacKinnon, and R. Pinkel, 2010: Long-range propagation of the semidiurnal internal tide from the Hawaiian Ridge. *J. Phys. Oceanogr.*, **40**, 713–736, doi:10.1175/2009JPO4207.1.

——, ——, J. Girton, T. S. Johnston, and G. Carter, 2011: Internal tides around the Hawaiian Ridge estimated from multisatellite altimetry. *J. Geophys. Res.*, **116**, C12039, doi:10.1029/2011JC007045.

——, ——, and ——, 2012: Mapping low-mode internal tides from multisatellite altimetry. *Oceanography*, **25**, 42–51, doi:10.5670/oceanog.2012.40.